

Visual Experimental and Numerical Investigations Around the VLM-1 Microsatellite Launch Vehicle at Transonic Regime

Henrique Oliveira da Mata¹, João Batista Pessoa Falcão Filho², Ana Cristina Avelar², Leonardo Motta Maia de Oliveira Carvalho², João Luiz F. Azevedo²

ABSTRACT: It is performed and presented an experimental and numerical investigation over the flow patterns around the forebody section of a microsatellite launch vehicle in development at Instituto de Aeronáutica e Espaço. The experimental investigation with a VLM-1 model in 1:50 scale is carried out at the Brazilian Pilot Transonic Wind Tunnel, located in the Aerodynamics Division of the mentioned Institute, using the classical *schlieren* flow visualization technique. *Schlieren* images are obtained for nominal Mach number varying from 0.9 to 1.01. Numerical simulation using Stanford's SU2 code is conducted together with the experimental investigation in order to improve the understanding of the complex physical phenomena associated with the experimental results of this particular regime. The combination of the 2 techniques allowed the assessment of some important aspects on the flow field around the vehicle in the conditions considered in this study, such as shock wave/boundary-layer interaction. The numerical simulation is also very important, allowing the quantification of some important parameters and confirming the shock wave formation patterns observed in the simulation when compared with the *schlieren* images. A good agreement regarding the position of the shock wave, when compared with the *schlieren* images, with a maximum error of about 6%, is observed over the VLM model.

KEYWORDS: Sounding rocket, Transonic Wind Tunnel, Experimental results, *Schlieren* images, CFD.

INTRODUCTION

The VLM-1 microsatellite launch vehicle is a project being developed at the Instituto de Aeronáutica e Espaço (IAE) since 2010 in partnership with the German Space Center (Deutsches Zentrum für Luft- und Raumfahrt e. V. — DLR) (Da Mata 2013). The idea was based on an up-to-date market analysis related to the applicability, frequency of launches, and price of microsatellites in the technological development. Among the applications the most important are the support and/or complementation of the present usages of large-scale satellites and the provision of better assistance for short-time revisiting spatial installations, allowing low-cost missions both related to launcher ground platform as well as design and manufacture of the prototype. The US Federal Aviation Administration (FAA) reports an average rate of 3 microsatellites launches per year, but other studies suggest more than 20 annual launches in a near future, creating a high demand that cannot be supplied anymore by old and costly large-scale projects, such as old missile-based large-scale Russian satellites and some expensive new projects like Angara, PSLV, and Falcon 1. A new era of microsatellite projects has emerged in the last 10 years, as confirmed by the ICBM-based vehicles from Russia, such as Dnepr, Cosmos 3M, and Start, as well as the American Pegasus. Therefore, with the development of the VLM-1 vehicle, the IAE has the possibility of putting Brazil into the promising market of microsatellites launching.

¹.Departamento de Ciência e Tecnologia Aeroespacial – Centro de Lançamento de Alcântara – Seção de Segurança de Vão – Alcântara/MA – Brazil. ².Departamento de Ciência e Tecnologia Aeroespacial – Instituto de Aeronáutica e Espaço – Divisão de Aerodinâmica – São José dos Campos/SP – Brazil.

Author for correspondence: Ana Cristina Avelar | Departamento de Ciência e Tecnologia Aeroespacial – Instituto de Aeronáutica e Espaço – Divisão de Aerodinâmica | Praça Marechal Eduardo Gomes, 50 – Vila das Acácias | CEP: 12.230-904 – São José dos Campos/SP – Brazil | Email: anacristina.avelar@gmail.com

Received: May 03, 2016 | **Accepted:** Nov. 22, 2016

The first configuration of the VLM was inspired by a successful Israeli rocket named Shavit. Although there are many configurations with different payloads, types of engines, and missions, the baseline vehicle consists of 3 stages and a payload that can vary from 140 to 350 kg. The main dimensional parameters of the adopted model configuration in 1:50 scale are defined in the scheme of Fig. 1. Its geometry is quite simple and aerodynamic, as it is expected a low drag coefficient because of the well-shaped nose and aspect ratio of 12.3 in a cylindrical body.

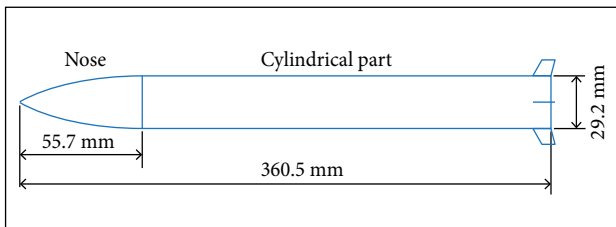


Figure 1. Main dimensions of the model adopted in 1:50 scale.

As the vehicle is developed in partnership with DLR, its evolution has certain particularities, both in organizational part and in research/manufacturing process. Some difficulties during the project must be solved by proving that the correct choice was adopted. One example is the fin conception. In the preliminary conception of the vehicle, no fins were predicted, and the rocket control would be done only by the nozzle. However, during the separation of the first and the second stages, the vehicle loses its control because the 1st-stage thrust is already terminated. In order to solve the problem, the Brazilian technical team proposed a set of fins, and it is up to the IAE staff to prove good stability characteristic of the vehicle, preserving a lower total drag.

In order to assess the aerodynamic behavior of the vehicle and to support other design decisions regarding many aspects of the rocket design, such as dynamic stability and aerodynamic loads, a test campaign was planned to take place in the Brazilian Pilot Transonic Wind Tunnel (TTP), located in the Aerodynamics Division (ALA) of IAE.

The good quality of *schlieren* image collection obtained during the tests, although very helpful for physical phenomenon assessment, was not considered sufficient for the deep understanding of the regime needed by the engineers during their design decisions. In order to improve such understanding, the examination of the problem with another methodology was taken into account. A useful tool that can give information about the whole flow field is based on the numerical techniques applied to the Reynolds-Averaged Navier-Stokes (RANS) equations. The

so-called Computational Fluid Dynamics (CFD) approach, which is nowadays sufficiently matured for rocket design purposes, proved to be the right choice. Stanford's SU2 code (Economon *et al.* 2016) was used to perform the numerical simulations. The RANS equations were solved using the Spalart-Allmaras model (Spalart and Allmaras 1992) to account for the turbulence closure required by the regime of the VLM-1 model (Wilcox 2006). The present paper presents and analyzes the *schlieren* images comparing them with numerical simulation results obtained with the SU2 code. The important insights obtained when using these tools are presented in the following sections.

Fluid flow forms complicated patterns that can only be completely understood with adequate and complementary approaches. The forming flow patterns can become quite unexpected, and it is almost never possible to predict the real flow characteristics relying just on classical aerodynamic theories. So other tools are always needed. One of the most efficient is Flow Visualization, or the direct observation of the flow field. Visualization is an important tool in establishing flow models as a basis for mathematical simplifications. It can be used for the direct solution of engineering problems, as well as to get insights about the concepts of fluid motion (Kline 1943). Although considered many times only as a qualitative method, Flow Visualization is of extraordinary value as it can reveal flow parameter behavior for the entire field. Conventional measuring techniques applied to real problems are generally very limited, because of both the model construction difficulties and the intrusiveness consequence, interfering with the flow pattern. Thus, it is worth noting the importance of experiments in flow visualization because it can assess flow properties for the entire field, which is almost impossible using conventional flow measurement techniques based on discrete points.

Since the advent of sufficiently powerful computers, in the last decades a considerable expansion in flow analysis has been observed as performed by the fluid mechanics academic community. Although CFD solutions can sometimes be considered inaccurate due to its deep numerical nature, it can still reveal some important information about the entire flow field. The best way one can imagine the application of this methodology is to verify its use for specific experimental study cases, improving the capabilities of both techniques: Flow Visualization and CFD. Therefore, the present study compared *schlieren* and CFD results in order to investigate the better physical phenomena in transonic regime for the VLM-1 vehicle model.

THEORETICAL APPROACH

Most of the simple geometry vehicles, such as the VLM-1, present a very typical aerodynamic flow pattern at transonic regime. Figure 2 shows the vehicle at typical transonic flow, when one can distinguish 4 different regions in which the boundary-layer (in dashed blue line) and the supersonic region (in dashed red line) with a shock wave at its end (in solid red line) play important roles. The distinctive regions are: (I) far upstream the vehicle the flow is at undisturbed condition; (II) approaching to the vehicle and along part of its nose the flow feels the presence of the model nose, rising the local pressure level as the boundary-layer starts developing from the nose tip; (III) to overcome the imposed geometry, at some point on the vehicle surface, and before the cone end, the Mach number is sonic because a supersonic region was created, ending with an approximately normal shock wave; (IV) after the shock wave the flow tends to return to the undisturbed condition.

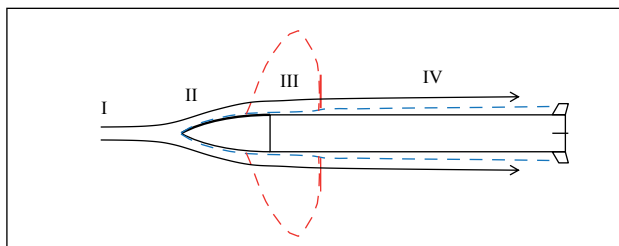


Figure 2. Diagram of the VLM-1 at typical transonic flow, showing the supersonic region and its interaction with the boundary-layer developed over the model surface.

The way the boundary-layer reacts by the impingent shock wave determines the flow locally. The interaction between the shock wave and the boundary-layer has been the topic of much scientific research since the 1950s (Dolling 2001). The diagram of Fig. 2 indicates how the boundary-layer grows significantly at the shock wave impinging point, which is caused by the obvious pressure level increase due to the shock wave. Depending on local characteristics of the flow, that is, whether it is laminar or turbulent, and the shock wave strength, the boundary-layer reacts differently, which may cause multiple shock wave formation, delta formation, as well as the boundary-layer may detach and later on being reattached or not.

Some special cases can be categorized considering weak or strong shock wave impinging over laminar or turbulent boundary-layer. At transonic regime, when the undisturbed flow condition is subsonic, a supersonic region will appear,

due to the geometric constraints, and its boundaries will be generally limited by a sonic line and by a normal shock wave at the end, where the supersonic flow returns to subsonic flow conditions. However, the boundary-layer along the vehicle surface has always a subsonic region very close to the wall, and it allows the characteristic parameters of the flow travel upstream. Across the shock wave, the boundary-layer will experience a sudden adverse pressure which will cause its growth locally. The supersonic flow external to the boundary-layer will react as if a geometric change had occurred, giving rise to compression and expansion waves. Depending on the strength of the shock wave, the boundary-layer will react differently, which will change the flow pattern outer the boundary-layer and the shock wave structure.

WEAK SHOCK WAVE IMPINGING ON LAMINAR BOUNDARY-LAYER

Figure 3 shows a diagram of the typical result of a weak shock wave impinging over a laminar boundary-layer. The geometry considered is the VLM-1 front part. In the figure, thin solid lines represent compression waves and the thick solid ones, the shock waves; dashed lines represent expansion waves and the dotted ones, sonic lines. In this case, the laminar boundary-layer is greatly affected by a shock wave and responds by increasing its thickness. Since the shock wave is weak, it is not capable of causing the boundary-layer complete detachment, although a small recirculation region may appear at the base of the stronger shock wave. The combination of weak shock wave with weak boundary-layer provides the appearance of a first shock wave followed by a number of weaker shock waves (Houghton and Carpenter 2003).

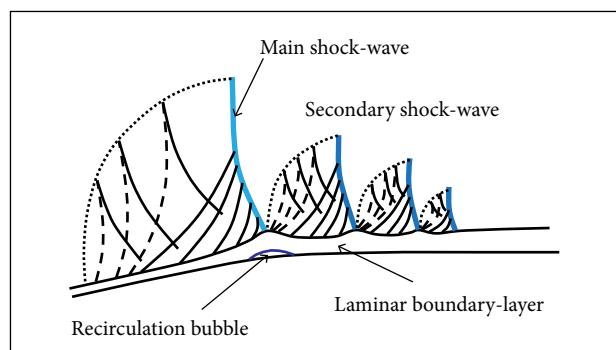


Figure 3. Weak shock wave/laminar boundary-layer interaction. Diagram modified from Houghton and Carpenter (2003).

As the flow travels along the vehicle surface, it reaches sonic condition at some point, and then it enters in a supersonic region where a sonic line and a shock wave are the constraints. Inside this region, outer of the boundary-layer, the flow behaves like a potential flow, where viscous forces are almost negligible. As the region expands geometrically, the flow outside the boundary-layer accelerates until a shock wave abruptly decelerates it to subsonic condition.

Nevertheless, inside the supersonic region, there are 2 facts worth noting. The first one is that, at the beginning, the boundary-layer growth is small and its outer limit defines a convex line for the flow above the boundary-layer. This frontier creates a series of expansion waves, which propagates upward until reaching the sonic line. As the expansion waves reaches the sonic line it returns from it as a compression wave, being propagated downward on the boundary-layer. The expansion and the compression waves are curved lines because of the so many interactions with all other waves.

The second fact is the presence of compression waves at some point downstream, because of the impressive boundary-layer growth, which is due to the adverse pressure rise imposed by the impinging shock. Depending on the strength of the shock wave, a recirculation bubble can occur.

The subsonic flow after the shock wave experiences a new expansion due to the accommodation of the boundary-layer outer limit, and it may accelerate to supersonic regime, as indicated in Fig. 3. Therefore, the same supersonic flow region pattern can be repeated, but now with smaller intensity. The same behavior is repeated until the flow has finally settled down to the undisturbed condition.

STRONG SHOCK WAVE IMPINGING ON LAMINAR BOUNDARY-LAYER

The main difference when compared with the last case is that the strong shock wave perturbs the laminar boundary-layer so much that it generally changes to turbulent, and sometimes it may cause even its complete detachment. Figure 4 shows in a diagram the flow pattern for this case. Because the first shock wave is very strong the other shock waves will disappear, only remaining a weak shock wave. A laminar recirculation bubble is likely to occur in this case, which normally will provoke the changing to turbulent flow regime ahead. It can be observed that the same pattern is found inside the supersonic regions where, whenever the outer flow undergoes, convex geometry expansion waves and concave geometry compression waves appear.

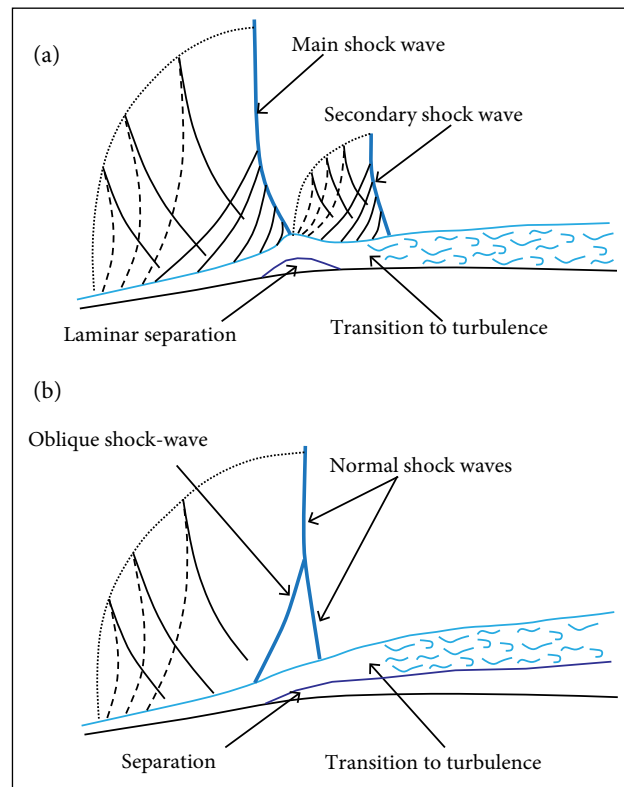


Figure 4. Strong shock wave impinging on laminar boundary-layer, resulting in turbulent boundary-layer: (a) With flow reattachment and (b) Completely separated flow. Diagrams modified from Houghton and Carpenter (2003).

STRONG SHOCK WAVE IMPINGING ON TURBULENT BOUNDARY-LAYER

Based on experiments, it is observed that the necessary force to detach a laminar boundary-layer is considerably lower than for a turbulent boundary-layer (Houghton and Carpenter 2003). For the present study cases, the most likely situation to occur in the presence of turbulent boundary-layer is the one with reattachment.

Some of the physical phenomena described herein were confirmed by the experiments undertaken in TTP, using the *Schlieren* Technique. Nevertheless, numerical simulations were also developed to better understand them by assessing other flow parameters that are not possible to observe just through *schlieren* images.

EXPERIMENTAL AND NUMERICAL APPROACHES

THE PILOT TRANSONIC WIND TUNNEL

The TTP is a scaled-down version (1:8) from an industrial transonic project idealized in the 1980s by the IAE to provide

Brazil with a transonic facility to support the aeronautical development of the country, reaching strategic goals of safety and up-to-date testing capabilities for new Brazilian aerospace projects. The transonic wind tunnel would be driven not only by a main compressor (continuously) but also by an injection system (intermittently), which would help to enlarge the operational tunnel envelope, without penalizing the installed power. Because of this new feature, a pilot transonic facility was also conceived in order to test this challenging idea (Falcão Filho *et al.* 2009). For several reasons, mostly related to budget restrictions, only the pilot facility design was completely built and it became fully operational in 2002.

TTP has also been built to train people and serve as a research tool for tests with profiles and models of simple geometries, like the aerospace vehicles. Figure 5a shows a view of the aerodynamic tunnel installed in a dedicated building, where one can see the tubing that connects the circuit with auxiliary compressors installed in another building to control tunnel pressure. Figure 5b presents the open plenum chamber showing the test section (in red) where the test article is installed and other tunnel components to establish the flow into the test section.

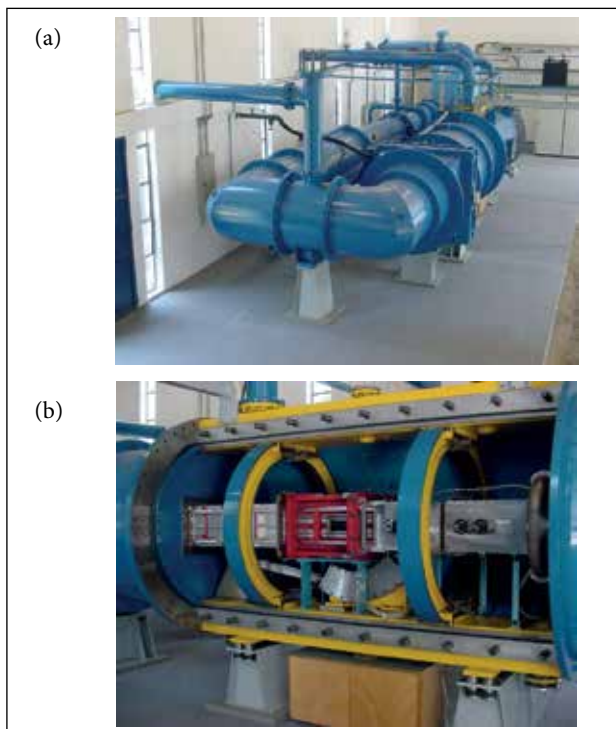


Figure 5. TTP installation: (a) Aerodynamic circuit, with 17 m long, showing tubing for auxiliary control systems; (b) Plenum chamber open showing the test section (in red), first and second throats.

TTP has a conventional closed circuit with test section of 0.30 m wide, 0.25 m high, and 0.81 m long, and it is continuously driven by a main axial compressor with 830 kW of power, attaining flows in the Mach number range from 0.2 to 1.2. An intermittent injection system operates in combined action with the main compressor reaching up to Mach number 1.3 during at least 30 s. Automatic controls of pressure (from 0.5 to 1.2 bar) and temperature guarantee stable operation to settle Mach and Reynolds numbers in the test section, which are the 2 parameters necessary to completely represent the flow for steady-state conditions (Barlow *et al.* 1999). In fact, the Reynolds number is quite difficult to settle in tests with small models, and even for industrial wind tunnels Reynolds numbers are normally of one order lower than those of real flight, requiring adaptations in the test procedure and in the model installation to diminish the so-called Reynolds number effects (Pope and Goin 1978).

Figure 6 shows a diagram of the plenum chamber with devices idealized to perfectly establish the flow into the transonic test section: the first throat which accelerates the flow coming from the stagnation chamber to the test section entrance; the slotted test section in which the article is mounted; the re-entry flap section which can change the angle and vary the mass flow through the slots; the second throat to adjust conditions whenever supersonic tests are performed; and the injector mixing chamber. There are ten injector beaks, which receive compressed air and operate in a choking condition at Mach number 1.9 to transfer momentum to the main stream. In Fig. 6 the curved arrows show the flow direction coming out from the test section and being re-admitted by the flaps by the pressure decrease due to Venturi effect. Normally the flow, represented by its streamlines, it deviates from the model in its proximity. In closed wall test section the streamlines are closer to the model than in real flight flow whilst in open wall test

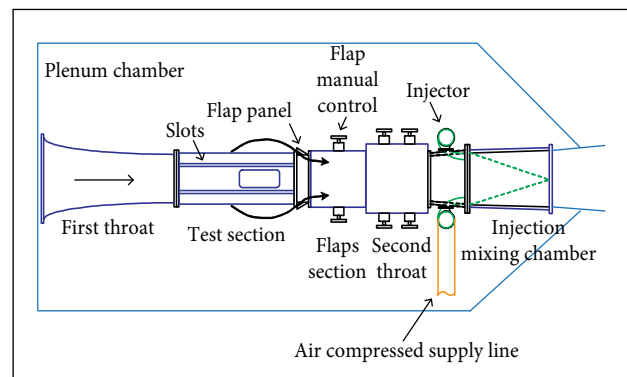


Figure 6. Detail of the plenum chamber inner parts.

section they are more distant from the model than in real flight. In both cases the perfect similarity between flow conditions in wind tunnel and in free flight are prevented. In a transonic semi-open wall test section, even with the flaps close, when the flow upstream the model feels its blockage it responds causing the streamlines to bulge out in an intermediate behavior, in some cases reproducing quite well the real flight condition (Goethert and Nelson 2007).

Figure 7 shows the tunnel operational envelope in terms of the numbers of Mach and Reynolds, for a typical chord of 27.4 mm, which represents 10% of the square-root of the cross sectional test section area (Davis *et al.* 1986). It is clear that the continuous operation of TTP goes up to Mach number 1.23 and to reach Mach number 1.3 it is necessary to use the injection system. The envelope describes all operational limits for the tunnel. It is important to emphasize that, for a fixed Mach number condition, it is possible to vary the Reynolds number, which is accomplished by varying the stagnation pressure of the test section. The Reynolds number variation can be used to give some insight about extrapolating procedures to the real flight condition for some characteristic parameters.

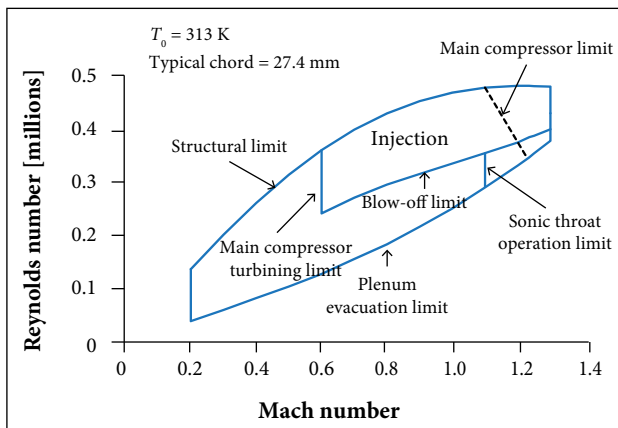


Figure 7. Operational envelope of TTP for stagnation temperature of 313 K and typical chord of 27.4 mm.

Some experiments undertaken in TTP were reported in Da Mata (2013), and they included determination of drag force with study of transition using Carborundum strips with different grit sizes, as stated in Pope and Goin (1978) from Mach number 0.3 to 1.15, and flow visualization using the *Schlieren* Technique to exploit the transonic regime from Mach number from 0.90 to 1.01.

Figure 8 shows the model installed inside the test section of TTP, from which the side wall was removed. It is possible

to see the longitudinal slots of the test section which will have its pressure equalized by the plenum chamber. The 3 basic objectives with the slots are to establish uniform transonic regime flow preventing choking, to diminish the shock and expansion wave reflections from the walls, and to control the mass flow through the walls to improve flow uniformity. The model is instrumented with a 6-component internal balance, and its diameter of 29.2 mm represents 0.9% of blockage area (ratio between the highest model cross sectional area and the test section area). According to Pope and Goin (1978), a blockage ratio below 1% assures negligible test section wall corrections, simplifying enormously the data reduction procedures. The model has four small fins at its base to allow the vehicle stabilization. For this particular test, a special device was used to fix the model in the sting support to move the model 30 mm upper from the central line of the test section, placing it practically at the end of the visualization window, allowing more free space to capture the shock wave formations.

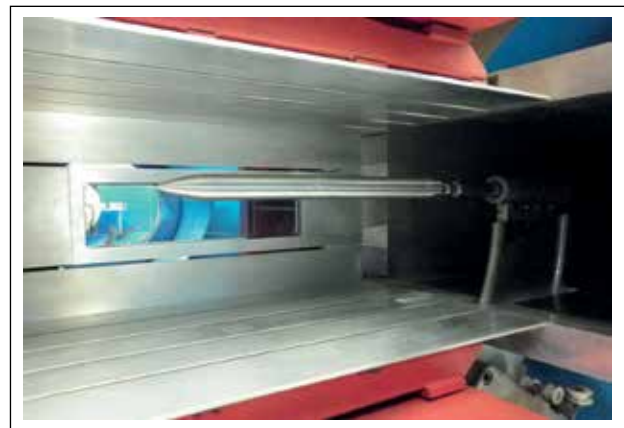


Figure 8. VLM-1 model in 1:50 scale installed in the TTP Test Section.

The TTP test section is relatively small and the scaled model constructed with 29.2 mm of diameter results in very low Reynolds numbers. The *schlieren* images were taken with the model without any transition strip and at 0° angle of attack. Therefore, it is expected that a laminar boundary-layer will extend for a relatively long region on the model surface. Table 1 shows the main parameters related to the test section of TTP for transonic regime, considering the characteristic length of 55.6 mm, which corresponds to the VLM-1 ogive length. Considering that the transition from laminar to turbulent flow in a flat plate will typically occur from 100,000 to 500,000, one can see that the boundary-layer will be laminar approximately

up to half-way along the ogive for all experiments. Depending on where the shock wave is located, it is expected local laminar or turbulent boundary-layer characteristics at the foot of the shock.

Table 1. Typical transonic test parameters undertaken in TTP, with corresponding Reynolds numbers related to the ogive length (55.6 mm).

Mach number	Stagnation pressure (kPa)	Stagnation temperature (K)	Re (thousands)
0.7	94	303	658
0.8	94	303	708
0.9	94	303	746
1.0	94	303	773
1.1	94	303	788

SCHLIEREN TECHNIQUE

The experiments were undertaken using the *Schlieren* Technique. The method is based on flow visualization of the light intensity difference as function of the local density gradient in the flow field. For example, high density gradients indicating shock waves around the test object can be visualized by different intensity of light scattered in a recording plane. Figure 9 shows a diagram of the basic physical installation used. The point light source located precisely at the focal point of the first parabolic lens forms a parallel light beam that crosses the test object region. Different density regions refract differently the light beam because of the refrangibility degree variation in the local medium. Therefore, the image on the recording plane will show the high density regions with shadow close to more illuminated areas. The *Schlieren* Technique uses another parabolic lens to converge light rays at the focal point, where a knife edge is approximated, and, as its location is altered, it changes the image contrast, as it blocks some of the light rays which were diverted from the focal point. The combination of the two parabolic lenses produces an image with illumination rate as function of density gradient. Figure 9 shows in dashed lines 2 light rays which experienced symmetric deflections because

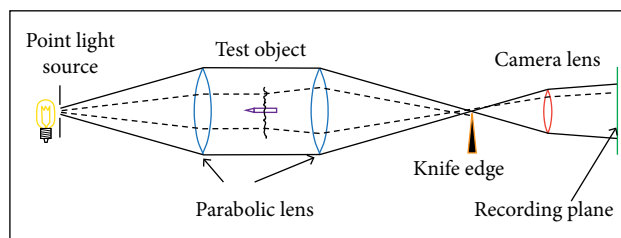


Figure 9. Installation diagram of the *Schlieren* Technique.

of density variation in the flow field. The knife selected one direction instead of the other to obtain an image contrast. Both lens work together to yield an image in which the luminosity is a function of the first derivative of the density in the field (Tropea *et al.* 2007). However, because of the difficulty in reducing the results to obtain density distribution in the field, the images are considered here only to determine the shock wave and expansion locations.

NUMERICAL SIMULATION

It is usual to use numerical simulations when trying to understand complex physical phenomena and experimental results. Since numerical simulations are not, typically, considered alone during important design decisions, some care is usually exercised by the CFD engineers to reduce the grounds for large errors in the results. Hence, typically, mesh independence studies and the enforcement of adequate convergence criteria are emphasized. The discussion about even the substitution of experimental results by numerical simulations is a modern theme, as stated by Kraft (2010), which redirects the debate by pointing both approaches as parts of an integrated solution to reduce the overall cycle time for development of aeronautical systems.

To simulate numerically for steady state condition the experimental configurations, the Navier-Stokes equations (Anderson *et al.* 1984) were solved by a RANS approach with a 2nd-order finite-volume approximation and using an implicit method. The turbulence effects were accounted for by using the Spalart-Allmaras model (Spalart and Allmaras 1992; Spalart 2000). To simulate the flow field around the fore-body region of the VLM-1 model and precisely capture shock waves, the SU2 open source computational code was used (Economou *et al.* 2016).

Although the boundary-layer developed over the model may be locally laminar, resulting in distinct interaction with the shock-wave, using the code for laminar condition is out of question, because the physical field is distinguished turbulent, and a laminar approach does not correspond to the physics. The authors must admit, however, that even the use of the Spalart-Allmaras model with a quadratic constitutive relation (Spalart 2000) may not represent the ideal situation for the present flow condition. Actually, probably no eddy-viscosity model would be really adequate in this case. The ideal situation would be to couple the eddy viscosity model with some transition model, such as, for instance, the Langtry-Menter model (Langtry and

Menter 2009; Halila *et al.* 2016). Unfortunately, however, the effort involved in the coding and validation of such an approach would be beyond the available resources here.

MESH INDEPENDENCE STUDY

Since CFD is highly dependent on numerical methods, errors are always included by the approximate nature of these numerical schemes. Numerical schemes are needed in different parts of the solver to deal with the complex fluid dynamic equations. Unfortunately, some of the errors brought by the numerical algorithm are intrinsic to these numerical schemes and cannot be directly reached by the user without further work in the original derivations. In an effort to minimize the errors included by these approximations, mesh independence studies are needed in order to isolate the influence of the mesh in the final solution.

Before proceeding with the actual simulations of interest, 5 meshes and their influence in the solution were studied. These grids had sizes varying from about 19,000 to approximately 1,000,000 internal hexahedral elements. During the study, 2 major issues were brought to the mesh independence study as practical constrains. The first one was concerned with spatial resolution of the shock-wave and the second was concerned with convergence. Spatial resolution of the shock wave was needed for better comparisons between the post-processing images and *schlieren* images. On the other hand, the grid could not be extremely fine. This refinement excess could add too much numerical stiffness to the solution and, as a consequence, the numerical stiffness would cause trouble when seeking for high quality steady state solutions. Table 2 shows the developed meshes used in the refinement analysis. In all cases, the $y^+ < 1$ for the first boundary-layer calculation point was observed, as prescribed by the turbulence model. The results in terms of shock-wave location and C_p distribution over the model body revealed practical convergence between the fine and the finer meshes.

Table 2. Number of elements in each mesh used during the refinement analysis.

Mesh name	Internal number of mesh elements
Badly refined	19,266
Coarse	32,393
Medium	131,946
Fine	735,513
Finer	1,172,222

In order to select the best mesh for the simulations, pressure coefficients results over the VLM model wall in the longitudinal direction from all meshes were compared with each other, along with a qualitative analysis of the shock wave resolution using Mach number contours. Figure 10 shows an example of the comparison using 3 meshes: (a) the poorest one (poorly refined according to Table 2), (b) the fine, and (c) the finer meshes. Mach number fields using the same range and number

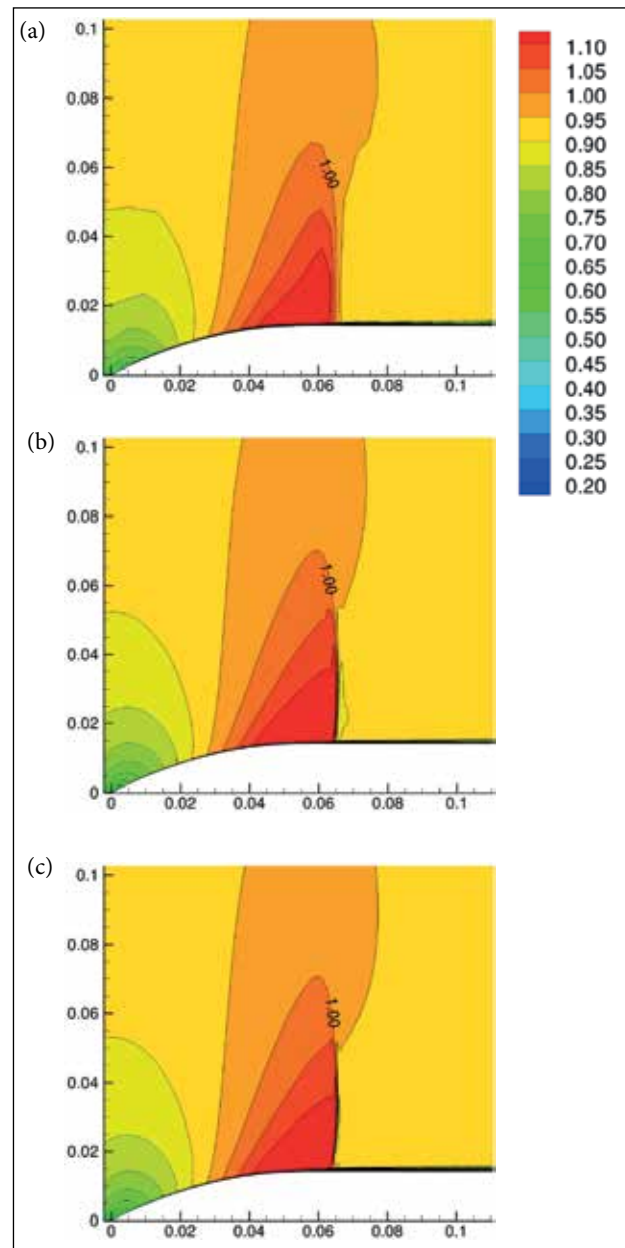


Figure 10. Mach number fields for 3 meshes: (a) Badly refined, (b) Fine, and (c) Finer meshes, according to the specification from Table 2.

of levels are plotted, as they reveal the lack of precision in Fig. 10a, and the good agreement between results from fine (Fig. 10b) and finer (Fig. 10c) meshes.

The finer mesh did not completely converged, only allowing four digits of decrease in the L_∞ norm of the density residue. The “fine” mesh was selected based on the shock wave location and thickness, and also on the convergence characteristics and computing time, presenting good shock resolution together with reasonable computational cost and convergence compared to the other meshes. Figure 11 shows the convergence history for the solution using the fine mesh for nominal free-stream Mach number of 0.9.

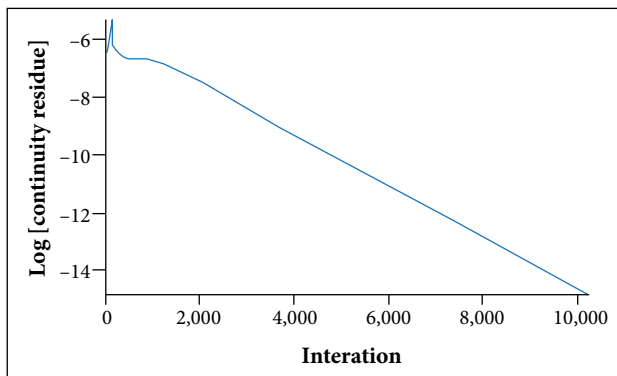


Figure 11. Convergence history for the continuity equation.

CHARACTERISTICS OF THE ADOPTED MESH

During the development of the computational mesh, some simplifications were adopted to make the problem tractable to the computing power available when compared to the full experimental configuration. These were:

- The tunnel walls were not represented as free-stream condition was applied to the flow. With a model blockage area ratio of 1%, practically no wall interference effects for zero angle of attack are expected.
- Since the fore-body region of the model is axisymmetric and the angle of attack for all cases was equal to 0° , the computational field could be restricted to 20° in the azimuthal direction with a simulation plane at each 1° , provided that symmetrical side plane conditions were imposed — previous simulations proved that 10° dihedral angle was enough by comparing it with a 20° solution.
- The model was represented without the fins at its base and the model geometry finishes at the end of the mesh, without the representation of the wind tunnel

sting support or a truncated geometry, considering that the flow phenomena at the model base will not affect the model fore-body region, which is the object of the present research.

Besides the symmetrical lateral plane conditions required by the dihedral created, over the model surface, non-slipping adiabatic flow conditions were imposed, and elsewhere far-field conditions were imposed. Although a 2-D mesh could be used because of the symmetrical characteristics of the problem, a 3-D approach is a better solution because of the inherent 3-dimensionality of the turbulence.

Figure 12 shows details of the adopted mesh. In Fig. 12a one can see the total mesh region of 10° of dihedral angle highlighting the central longitudinal plane and 2 transversal planes (in green) at the tip and base of the model. The far-field limit is located about 170 diameters or 14 model lengths. Figure 12b shows detail of a longitudinal plane in the model region, delimiting model wall from its tip at (0.000 m; 0.000 m) and its base at (0.360 m; 0.0146 m), highlighting the point clustering in the fore-body region. Figure 12c shows the detail of the fore-body region showing the point clustering normal to the body wall to represent the boundary-layer, according to the requirement of the turbulent model ($y^+ < 1$), with the first point at 1×10^{-6} m and a stretching of 17%.

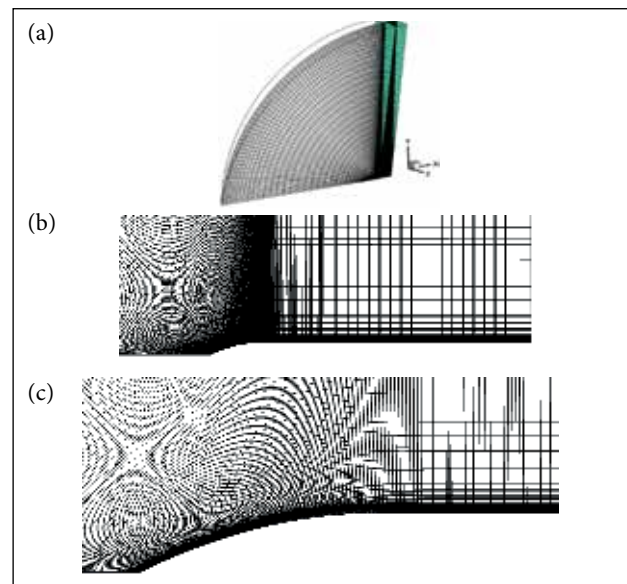


Figure 12. Details of the numerical mesh: (a) Total view with far-field distant 170 diameters; (b) Longitudinal plane detailing the model with 0.36 m of length and showing the regions of calculating point clustering; (c) The model fore-body detailing clustering close to the model wall to capture the boundary-layer.

RESULTS

Table 3 shows 12 of the main tests run in TTP to obtain *schlieren* images, along with the main test parameters with standard deviations related to the test section conditions. For some tests, numerical simulation was performed with the SU2 code aiming comparisons. Since the tests were carried out using supersonic first-throat, the Mach number informed

by the control needed correction, as it is shown in the Table 3. The study cases encompassed the relevant Mach number range in the transonic regime, and they were limited by the good quality of the available *schlieren* images, as allowed by the visualization window.

Figure 13 shows *schlieren* photographs from the tests undertaken in the TTP from free-stream Mach number from 0.8777 to 0.9893. The model was shifted about half diameter

Table 3. Main parameters related to test section condition of the tests performed with VLM-1 in TTP.

	Nominal Mach number	Corrected Mach number	Stagnation pressure (kPa)	Stagnation temperature (K)	Reynolds number ($\times 10^{-3}$)	Numerical simulation
1	0.90	0.8777 ± 0.0011	91.71 ± 0.14	306.29 ± 0.10	710.8	Yes
2	0.91	0.8869 ± 0.0009	91.93 ± 0.31	308.04 ± 0.09	710.3	Yes
3	0.92	0.8968 ± 0.0008	91.67 ± 0.10	308.59 ± 0.12	709.7	Yes
4	0.93	0.9069 ± 0.0008	91.62 ± 0.12	309.17 ± 0.09	710.7	Yes
5	0.94	0.9164 ± 0.0008	91.57 ± 0.06	309.57 ± 0.08	711.9	Yes
6	0.95	0.9272 ± 0.0008	91.66 ± 0.20	310.18 ± 0.16	713.8	Yes
7	0.96	0.9382 ± 0.0009	91.67 ± 0.12	310.20 ± 0.08	716.6	Yes
8	0.97	0.9475 ± 0.0008	91.72 ± 0.23	310.41 ± 0.08	718.8	No
9	0.98	0.9589 ± 0.0007	91.64 ± 0.06	310.75 ± 0.07	719.9	No
10	0.99	0.9688 ± 0.0007	91.67 ± 0.04	310.70 ± 0.07	722.6	No
11	1.00	0.9789 ± 0.0009	91.73 ± 0.12	310.78 ± 0.07	725.1	No
12	1.01	0.9893 ± 0.0009	91.81 ± 0.29	311.00 ± 0.09	727.3	No

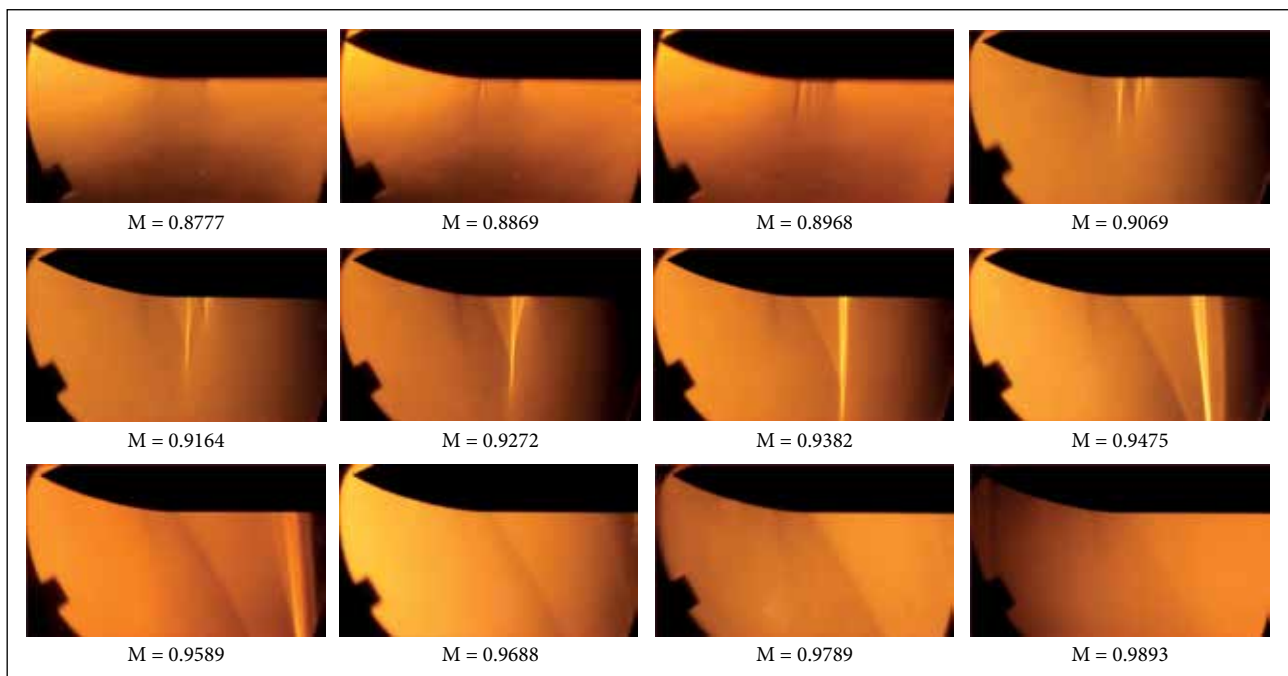


Figure 13. *Schlieren* photographs of tests with VLM-1 in TTP for different free-stream Mach numbers.

up from the test section center-line to attain a wider space of visualization. The proximity from the upper wall of the tunnel was about 3 model diameters which did not significantly influence the effects of the wall presence. It is important to note that, as it is common in *schlieren* images, in order to obtain a better contrast in the picture, the adjustment of the system caused small shadow effects in some regions of the photograph that do not represent density changes in the flow field.

As the vehicle front-body has aerodynamic shape, the *schlieren* photographs did not show interesting aspects until near free-stream Mach number of 0.8777, as it can be seen in Fig. 13. Therefore, the critical Mach number probably occurs a little lower than Mach number of 0.8777. At this Mach number condition, it is possible to distinguish a darker region starting before the nose end and finishing some distance after the cylindrical part of the vehicle. Numerical simulation will help to investigate better this condition in further studies.

For Mach number of 0.8869, the presence of a small shock wave formation near the nose end can be observed. In fact the formation looks like a main shock wave followed by a secondary weaker one, as discussed in the section “Theoretical Approach” for laminar flow. The Reynolds number for this Mach number condition is about 740,000 related to nose length, suggesting the existence of turbulent flow conditions. However, it is difficult to guarantee this condition since it is an expansion region and the local acceleration of the flow with a non-adverse pressure gradient contributes to its stabilization.

For Mach number of 0.8968, the main shock wave becomes stronger and it is followed by 3 secondary shock waves. The shock waves perceived at free-stream Mach numbers of 0.8869 and 0.8968 are normal to the local body surface and their feet are straight, indicating small growth in the boundary-layer thickness. This pattern resembles in some way the prediction shown in Fig. 3.

For Mach number of 0.9069, the pattern changes to a stronger main shock wave followed by a secondary one, which was formed by the collapse of the secondary shock waves, observed at Mach number of 0.8968. The shock waves are located in the cylindrical part of the model, and so they are normal to the free-stream flow. It is important to note that, now, the shock wave feet have lambda shape denouncing compression waves due to the growth of the boundary-layer thickness. This pattern resembles the prediction shown in Fig. 4a. In this case, it is possible that the boundary-layer experienced a recirculation bubble or even detachment. It is

worth noting how the shock wave formation pattern changes from Mach number from 0.8777 to 0.9069 and, even, for higher Mach numbers.

For Mach number of 0.9164, the pattern is repeated but the shock waves are stronger, and, finally, for Mach number of 0.9272, the 2 shock waves collapse in one stronger shock wave with its foot in a lambda shape. For Mach numbers from 0.9382 to 0.9589, the strong and unique shock wave formation progresses and advances downstream. For Mach numbers from 0.9688 to 0.9893 the available window does not show the shock wave formation because it traveled downstream. It is noteworthy, from the results for Mach number of 0.9164 and, repeatedly, for higher Mach numbers, a clear contrast in the pictures, starting before the nose end and finishing just after the nose end, which shows the limits of a supersonic expansion at the same location.

Figure 14 shows the numerical simulation results in terms of Mach number contours for free-stream Mach number of 0.85. In the figure, one should note the iso-Mach line legends being increased by 0.02. The maximum Mach number determined in the field is about 1.00, thus representing the critical free-stream flow condition. The nose has aerodynamic shape, which contributes to smooth flow acceleration along the model body. Starting at this free-stream condition and increasing the Mach number, it is expected a shock wave formation and an expressive rise of the drag coefficient, as the flow experiences transonic regime.

Figure 15 shows the numerical simulation result in terms of Mach number contours for free-stream Mach number of 0.8777. The maximum Mach number observed in this case was 1.067, corresponding to the first supercritical condition of the studied cases. It is already possible to realize that the sonic Mach-line underwent a small disturbance at approximately 0.050 m, which indicates initial formation of a shock wave, too

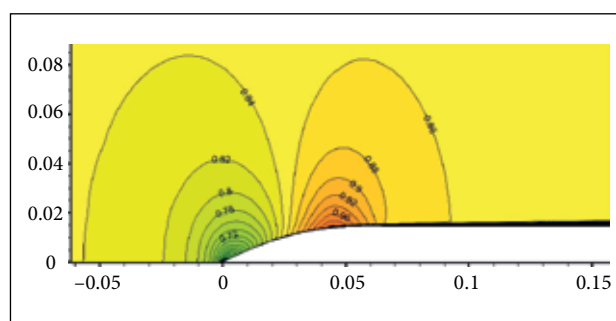


Figure 14. Mach number contours for free-stream Mach number of 0.85, corresponding to critical conditions.

weak to be noticed by *schlieren* images, as shown in Fig. 13. In Figs. 14 and 15, one can see the accumulation of iso-Mach lines close to the model wall due to the deceleration of the flow, and the region grows along the model surface because of the boundary-layer thickness growth.

In Fig. 16, it is shown the pressure field for free-stream Mach number of 0.8869. As the isobaric lines cross the boundary-layer on the model surface, there is no accumulation of lines, as those observed in Mach number contour plots. A shock wave formation at about 0.0500 m from the model tip is clear. A careful observation of the *schlieren* image for Mach number 0.8869 (Fig. 13) will indicate the main shock wave at a distance of 0.0519 m and the secondary at 0.0541 m. As previously discussed, no eddy-viscosity model can predict transition, or relaminarization; therefore, the laminar 2-shock-wave formation observed in the *schlieren* image could not be numerically represented. However, the comparison of the main shock wave location measured from the model tip in both techniques had a disagreement of only 3.8%.

As discussed, it was already expected that the laminar multiple shock wave formation could not be predicted by the present

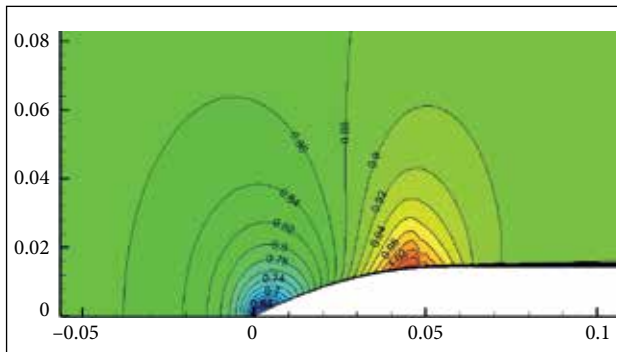


Figure 15. Mach number contours for free-stream Mach number of 0.8777.

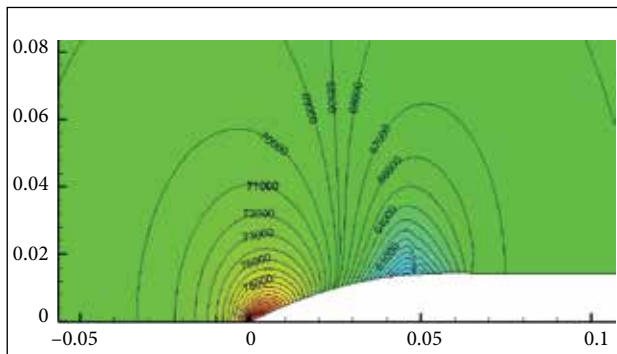


Figure 16. Numerical simulation of pressure field for free-stream Mach number of 0.8869.

numerical simulation approach. However, observing Fig. 13, one can see that the laminar shock formation will practically end at Mach number 0.9272, when the shock wave collapses into a unique shock wave formation. Figure 17 compares both numerical and *schlieren* image results for free-stream Mach number $M_\infty = 0.9272$, where one can see a good prediction of the shock wave location through the numerical simulation, with an error of 6.2%. In general, it is possible to visualize that the numerical result overpredicts the physical phenomena, such as sonic line, supersonic region, and shock wave location. The shadowed expansion region in the *schlieren* image is followed by a more illuminated area, which would indicate compression wave formation region, but this fact was not demonstrated by the numerical result. Besides, the numerical simulation could not predict the complex formation at the shock wave foot, where the boundary-layer has an important role, most certainly due to the lack of resolution of the boundary layer.

Figure 18 shows the same results for free-stream Mach number of 0.9382. In this case, it is possible to note a better comparison between results, and the error in the shock wave location predicted by numerical calculation was 3.7%. Isobaric line representing the sonic condition (dashed red line) had a noticeable increase in the field. It is interesting to observe that the shock wave in the *schlieren* image is a straight line while the same shock wave in numerical simulation has a curvature, indicating some effect from the boundary-layer.

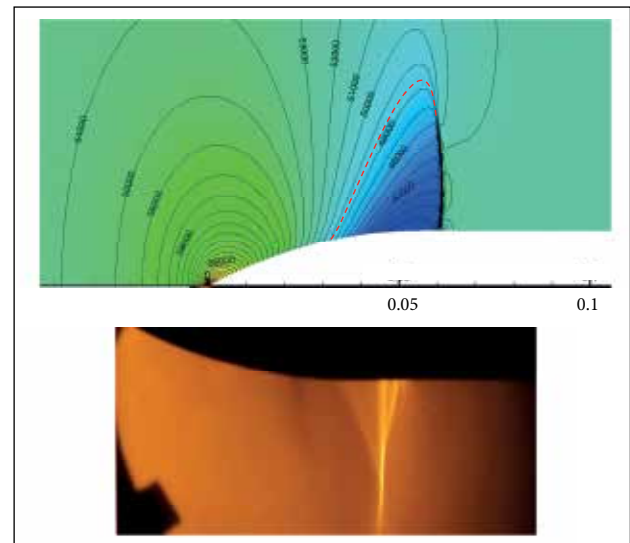


Figure 17. Numerical simulation result of pressure contours compared with *schlieren* image for free-stream Mach number of 0.9272. The isobaric line increases by 1,000 Pa. Dashed red line highlights isobaric line related to sonic condition.

A very important issue is the role of the turbulence in the flow field. Figure 19a shows turbulent viscosity contours. Here, eddy viscosity is made dimensionless by the free-stream viscosity coefficient. The accumulation of lines close to the model wall indicates the boundary-layer development. Although the present approach implies that the flow is fully turbulent from the beginning, it is clear that eddy viscosity generation occurs inside the boundary layer. Hence, close to the model tip, since the

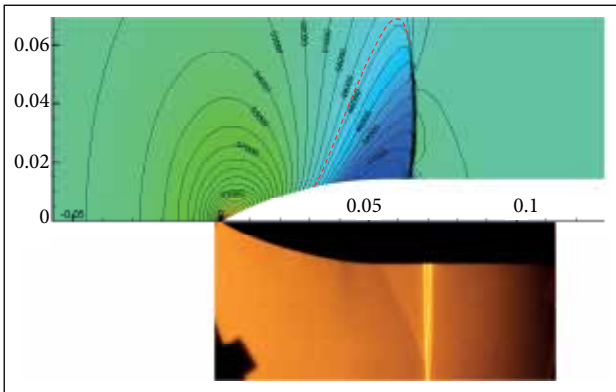


Figure 18. Numerical simulation result of pressure contours compared with *schlieren* image for free-stream Mach number of 0.9382. The isobaric line increases by 1,000 Pa. Dashed red line highlights isobaric line related to sonic condition.

boundary-layer is very thin, turbulent effects are almost negligible. As the boundary layer grows along the body, so does the eddy viscosity coefficient, which reaches a value equal to 320 times the viscosity coefficient of free-stream far-field. This increase occurs just downstream of the shock wave impingement point, hence, indicating a tremendous increase in turbulent effects together with the growth of boundary-layer due to shock wave interaction.

It is also important to note how the turbulent activity decreases when the flow experiences acceleration by expansion in the supersonic region. Figures 19b and 19c show a detailed view of the shock wave foot, highlighting the iso-lines of turbulent viscosity and also plotting the velocity vectors in the flow field. It is notorious the increase of the boundary-layer thickness after the shock wave along with the turbulent viscosity. A detailed inspection of the boundary-layer indicated its thickness to be about 0.5 mm just before (and 0.8 mm just after) the shock wave, using the criterion of 95%.

CONCLUSION

VLM-1 model in scale 1:50 was tested in the TTP of IAE, and very important results obtained with *schlieren*

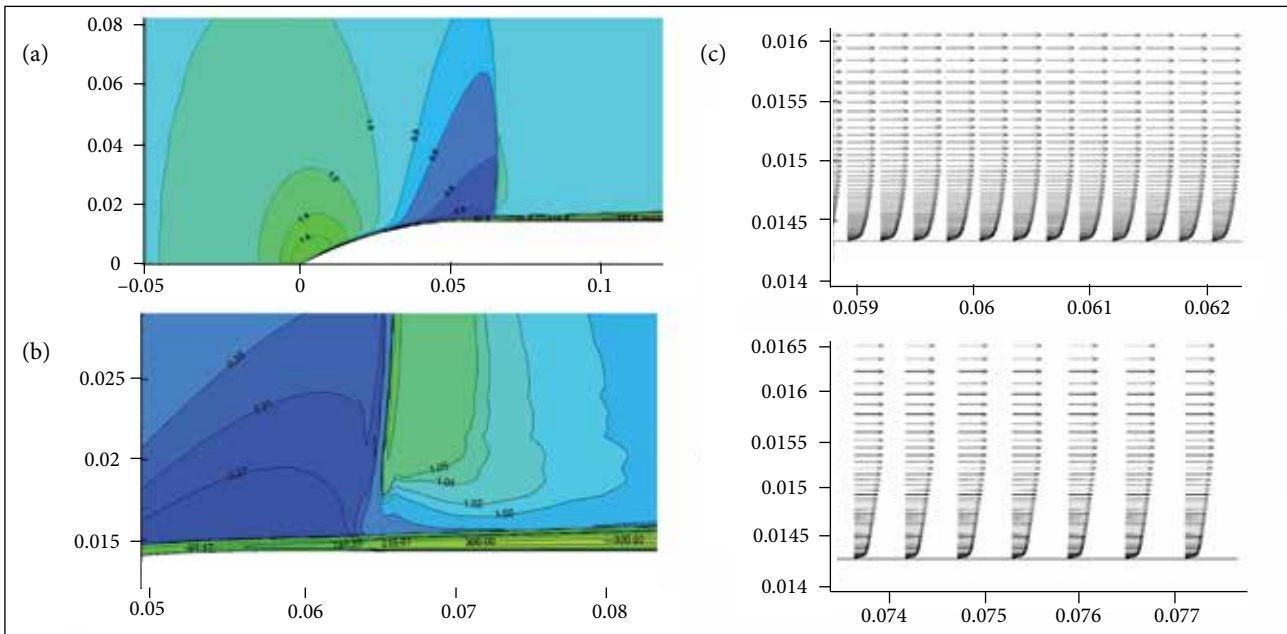


Figure 19. (a) Numerical simulation result of turbulence field for free-stream Mach number of 0.9382; (b) Detail of the base of shock wave with turbulence field (the iso-lines of turbulent viscosity were determined by dividing local values by the value at free-stream condition); (c) Velocity profiles before and after the shock wave (the boundary-layer thickness at $x = 0.060$ m is 0.00055 m, and at $x = 0.076$, 0.00094 m).

visualization technique in transonic regimes were presented and discussed. Shock wave formation over the model could be observed as the Mach number increased from 0.8777 to 0.9893. Because of the aerodynamic shape of the model ogive, *schlieren* image showed shock wave formation starting at free-stream Mach number of 0.8869. Typical laminar shock wave/boundary-layer interaction was perceived by multiple shock wave formation.

Numerical simulation performed by SU2 using the same flow conditions for some of the experiments allowed to observe other variables from the physical field, such as pressure, Mach number, turbulent viscosity, and velocity vectors. Numerical search indicated free-stream critical Mach number to be about 0.85. Although numerical simulation could not predict well the laminar and transition behavior of the boundary-layer, it was possible to observe good agreement of the shock wave distance location with a maximum error of about 6% from model tip. The numerical simulations were very helpful to understand *schlieren* images obtained and to quantify some important flow parameters.

REFERENCES

- Anderson DA, Tannehill JC, Pletcher RH (1984) Computational Fluid Mechanics and heat transfer. Washington: Hemisphere Pub. Corp.; New York: McGraw-Hill.
- Barlow JB, Rae WH, Pope A (1999) Low-speed wind tunnel testing. 3rd ed. New York: Wiley.
- Da Mata HO (2013) Procedimento Experimental para Análise Aerodinâmica do Veículo Lançador de Microsatélite VLM-1 (Undergraduate thesis). São José dos Campos: Instituto Tecnológico de Aeronáutica.
- Davis MW, Gunn JA, Herron RD, Kraft EM (1986) Optimum Transonic Wind Tunnel. Proceedings of the 14th AIAA Aerodynamic Testing Conference; West Palm Beach, USA.
- Dolling DS (2001) Fifty years of shock-wave/boundary-layer interaction research: what next?. AIAA J 39(8):1517-1531. doi: 10.2514/2.1476.
- Economou TD, Palacios F, Copeland SR, Luckaczyk TW, Alonso JJ (2016) SU2: an open-source suite for multiphysics simulation and design. AIAA J 54(3):828-846. doi: 10.2514/1.J053813
- Falcão Filho JBP, Avelar AC, Reis MLCC (2009) Historical review and future perspectives for Pilot Transonic Wind Tunnel of IAE. J Aerosp Technol Manag 1(1):19-27. doi: 10.5028/jatm.2009.01011927
- Goethert BH (2007) Transonic Wind Tunnel testing. Mineola: Dover Publications.
- Halila GLO, Bigarella EDV, Azevedo JLF (2016) Numerical study on transitional flows using a correlation-based transition model. J Aircraft 53(4):922-941. doi: 10.2514/1.C033311

ACKNOWLEDGEMENTS

The authors gratefully acknowledge the Agência Espacial Brasileira (AEB) for the support for this research. Partial support was also provided by the Conselho Nacional de Desenvolvimento Científico e Tecnológico (CNPq), under Research Grants No. 309985/2013-7 and 308829/2015-8. The authors are also indebted to the partial financial support received from the Fundação de Amparo à Pesquisa do Estado de São Paulo (FAPESP), under Research Grant No. 2013/07375-0.

AUTHOR'S CONTRIBUTION

Mata HO and Falcão Filho JBP conceived and conducted the experiments; Avelar AC participated in the experiments as well. The numerical simulations were conducted mainly by Falcão Filho JBP and Carvalho LMMO; Azevedo JLF participated in the discussion of the results and in the writing of the main text, which was done mostly by Falcão Filho JBP, with the participation of the other authors.

Houghton EL, Carpenter PW (2003) Aerodynamics for engineering students. 5th ed. Amsterdam: Elsevier.

Kline SJ (1943) Flow Visualization. Internet movie from the National Committee for Fluid Mechanics Films under a grant from the National Science Foundation; [accessed 2017 Jan 13]. <http://web.mit.edu/hml/ncfmf.html>

Kraft EM (2010) After 40 years why hasn't the computer replaced the wind tunnel?. International Test and Evaluation Association Journal 31:329-346.

Langtry RB, Menter FR (2009) Correlation-based transition modeling for unstructured parallelized Computational Fluid Dynamics codes. AIAA J 47(12):2894-2906. doi:10.2514/1.42362

Pope A, Goin KL (1978) High-speed wind tunnel testing. New York: John Wiley & Sons

Spalart PR (2000) Strategies for turbulence modelling and simulation. Int J Heat Fluid Flow 21(3):252-263. doi: 10.1016/S0142-727X(00)00007-2

Spalart PR, Allmaras SR (1992) An one-equation turbulence model for aerodynamic flows. Proceedings of the 30th Aerospace Sciences Meeting and Exhibit; Reno, USA.

Tropea C, Yarin AL, Foss JF (2007) Springer handbook of Experimental Fluid Mechanics. Berlin: Springer.

Wilcox DC (2006) Turbulence modeling for CFD. 3rd ed. La Cañada: D. C. W. Industries.